

Design Optimization and Performance Comparison of Two Linear Motor Topologies With PM-Less Tracks

S. R. Aleksandrov¹, T. T. Overboom, and E. A. Lomonova

Electromechanics and Power Electronics Group, Department of Electrical Engineering, Eindhoven University of Technology, 5612AZ Eindhoven, The Netherlands

An essential requirement for a long-stroke linear motion system is a low-cost and robust track. To allow the implementation of a linear motor topology in such application, passive tracks, consisting no rare-earth material, are recommended to reduce the price. This paper presents a comparison between two linear motor topologies with permanent magnet (PM)-less tracks: e.g., linear induction motor (LIM) and linear flux-switching permanent magnet motor (LFSM). These motors are benchmarked to a linear permanent magnet synchronous motor (LSM), which merits itself for high force density. The LIM and the LFSM are optimized for maximized continuous force while considering the same footprint as the LSM. The optimization is based on a multiphysical model containing an analytical representation of the magnetic field distribution, force production, power losses, and thermal the behavior of both structures. The obtained parameters are used to compare different configurations of both motors to the LSM. The results of the comparison show that at the price of higher losses, both topologies have comparable thrust force to the LSM.

Index Terms—Design optimization, electric machines, electromagnetic analysis, electromagnetic modeling, induction motors, permanent magnet motors.

I. INTRODUCTION

THE linear permanent magnet synchronous motor (LSM) is the preferable choice for linear motion applications when high force density is the main requirement. However, in a moving primary configuration, the main drawback of this motor is the relatively expensive track caused by the extensive usage of rare-earth materials. This limits the viability of these motors, especially for long-stroke applications, such as storage or airport transportation lines where the main prerequisite is a low-cost, passive and robust track.

Therefore, two alternative motor topologies are studied in this paper, namely a linear induction motor (LIM) and a linear flux-switching permanent magnet motor (LFSM).

Considering the price of the track as the main requirement, the LIM is the most attractive one. Conventional configurations have a conducting plate (aluminum or copper) as a secondary, which is mounted on a solid iron plate. Having no permanent magnets (PMs) in their construction, the LIMs do not have any cogging forces, which results in low force ripples. However, this reduces the efficiency and leads to a low power factor, which results in an increased inverter rating and therefore costs. Furthermore, the absence of rare-earth materials also limits the generated propulsion force.

Another attractive alternative is the LFSM, which also has a passive secondary, but is made of laminated silicon steel. The track is constructed as a teeth structure. Reluctance paths created by these teeth define the magnetic circuit of this motor. The LFSM's mover incorporates a limited amount of rare-earth materials, which significantly improves

its force generation capabilities. This construction combines the advantages of high force density of the brushless linear motors with the robust structure of the switched reluctance motor's passive track. The PM-biased primary generates significant cogging forces and therefore increases the force ripples [1].

Despite their early origins, the LFSM topology is still considered as a novel type in the industry, and the research on this topic is limited [2], [3]. Most of the available designs are directly derived from their rotary counterparts, which makes the direct comparison between the LIM and the LFSM very difficult. As an addition, the existing design solutions for the LIM differ very much from each other, as they are implemented in different applications. LIMs having short movers and therefore relatively small volume [4], [5] are designed with a lower thrust, compared with designs with much larger overall dimensions [6]–[8]. However, both the LIM and the LFSM are considered to be promising alternatives to the LSM for long-stroke applications because of their cheaper and more robust tracks.

In this paper, a comparative study on LIM and LFSM topologies is performed. To allow a fair comparison, semi-analytical methods are used to predict their performance and to obtain optimal design solutions within the footprint of a benchmark LSM topology. The motor configurations are optimized for maximum continuous force, accounting for the magnetic and thermal limitations of both LIM and LFSM. The results are used for comparison with the performance of the LSM topology.

In Section II, the analyzed topologies, i.e., LFSM and LIM, are presented together with the benchmark LSM topology. Section III discusses the methods used for modeling the topologies. In Section IV, the design optimization considerations are presented and the results are discussed. Finally, conclusions are presented in Section V.

Manuscript received March 18, 2018; revised May 4, 2018; accepted May 12, 2018. Corresponding author: S. R. Aleksandrov (e-mail: s.alexandrov@tue.nl).

Color versions of one or more of the figures in this paper are available online at <http://ieeexplore.ieee.org>.

Digital Object Identifier 10.1109/TMAG.2018.2837746

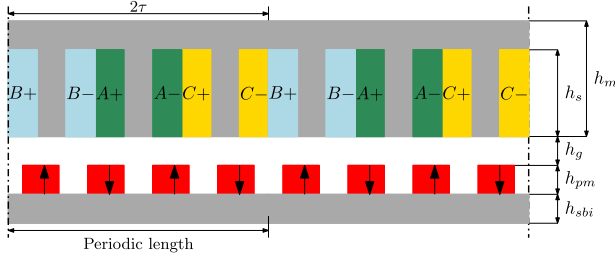


Fig. 1. Periodical section of a three-phase LSM.

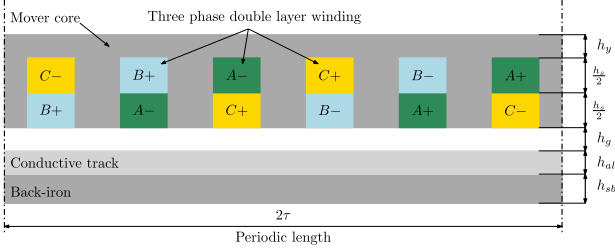


Fig. 2. Periodical section of a three-phase LIM with flat secondary.

II. ANALYZED TOPOLOGIES

In Fig. 1, one periodical section of the LSM, used as a reference for this paper, is shown. It represents a typical LSM configuration consisting of a three-phase coil unit and an infinitely long static array with axial magnetized permanent magnets. The thrust generation is a result of a traveling magnetic field produced by the armature windings and an array of magnetic poles. Usually, these motors are designed with concentrated coils, aiming for good manufacturability and short end-windings.

The construction of the analyzed LIM includes a moving three-phase coil primary with distributed windings and an infinitely long stator, made of flat aluminum mounted to an iron plate (Fig. 2). As the power factor of the LIM tends to be low and the magnetizing current tends to be significant, double layer windings are more beneficial because of their shorter end turns, as compared with single layer windings. A main advantage of this motor is its PM-less conductive passive secondary. The flux density in the airgap generates a traveling wave, which varies sinusoidally in both space and time. Reducing the electromagnetic problem to simple terms, it becomes one of relative motion between the primary magnetic field and the conductive secondary. While the secondary itself does not contain any sources of magnetic field, it experiences significant eddy-current effects, leading to substantial power losses, which cannot be neglected.

In Fig. 3, one periodical section of the analyzed LFSM topology is shown. The moving part incorporates the primary core, six tangentially magnetized permanent magnets, and two three-phase coil groups. The windings of this motor are concentrated and each magnet is placed in the center of a single coil. The track is also passive, as is the case for the LIM, but due to the reluctance nature of this motor, it is constructed as a salient structure with teeth and is made from laminated silicon steel. The principle of thrust force production results

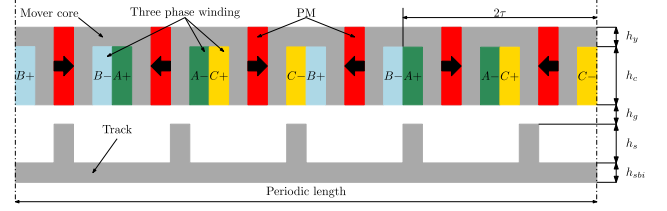


Fig. 3. Periodical section of a three-phase, 6/5 pole LFSM.

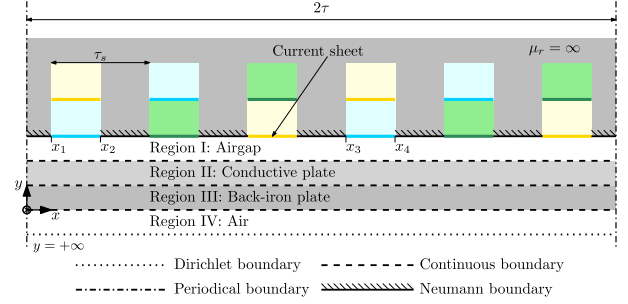


Fig. 4. LIM topology: division in regions and considered boundary conditions.

from the interaction between multiple magnetic excitation sources, e.g., armature currents, permanent magnets, and the salient ferromagnetic track. Hence, the variable airgap permeance is of a significant role in this type of motors. To obtain a phase flux linkage similar to that of the LSM, the used winding layout is three phase, and certain slot-tooth combinations are preferred. The 6/5 configuration is chosen for this comparison to eliminate distortions caused by even-order or third-order harmonics [9].

III. MODELING PRINCIPLES

A. Topology Assumptions and Division in Regions

Excluding the longitudinal end-effects, the topology of the LIM is periodical in the tangential direction. Therefore, complex harmonic method is a suitable semi-analytical modeling technique, where the magnetic field distribution can be obtained while accounting for the eddy-current effects in the conductive secondary [10]. The periodical section of the LIM is represented in a 2-D Cartesian coordinate system and is divided into rectangular regions in the xy plane, as shown in Fig. 4. By considering the primary core as infinitely permeable, the model is reduced to four main regions: Region I encloses the airgap between the mover and stator, while Region II contains the secondary conductive sheet, Region III represents the back-iron plate, and Region IV is used to model the air underneath the motor. The slotting of the primary is accounted for by adjusting the effective airgap length using Carter's coefficient. By reducing the conductivity of the conductive plate, the transverse end effects are included in the analysis [11].

As the material properties of both the mover and the track of LFSM vary in the x -direction, a hybrid analytical method, which combines harmonic modeling (HM) with magnetic equivalent circuit (MEC) [12], is chosen for this topology. The

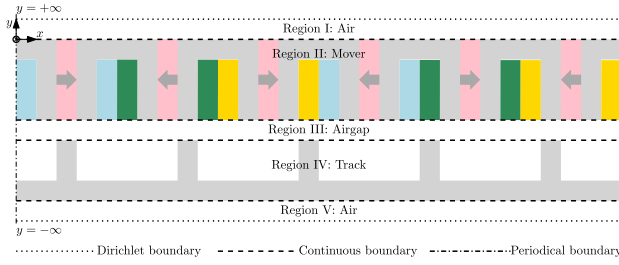


Fig. 5. LFSM topology: division in regions and considered boundary conditions.

topology of the LFSM is divided into five regions, as shown in Fig. 5. The harmonic method is used for the field description in Regions I, III, and V as these are periodical in the x -direction and they represent the free space over the mover, the airgap, and space beneath the secondary, respectively. Regions II and IV are modeled using the MEC, and they represent the mover and the track, respectively. To allow coupling between different regions and to increase the accuracy of the model, each of these MEC-regions is discretized, as is explained in Sections III-E and III-G.

B. Harmonic Modeling

The harmonic method is based on an analytical solution of the magnetic vector potential A_z expressed by Fourier series. It is obtained by applying the method of separation of variables, valid only in orthogonal domains with linear material properties. It is assumed that the magnetic flux density has only x and y components, while the vector potential has component in the z -direction only.

In a region with no conducting materials and no sources, e.g., Regions I and IV in the LIM and Regions I, III, and V in the LFSM, the vector potential solution has to satisfy the Laplace equation

$$\frac{\partial^2 A_z}{\partial x^2} + \frac{\partial^2 A_z}{\partial y^2} = 0. \quad (1)$$

When conducting materials are present in a particular region, e.g., Regions II and III in LIM, the time-varying field induces currents. These currents are related to the vector potential by the diffusion equation

$$\frac{\partial^2 A_z}{\partial x^2} + \frac{\partial^2 A_z}{\partial y^2} = \mu_0 \mu_r \sigma \frac{\partial A_z}{\partial t} \quad (2)$$

where σ and μ_r are the conductivity and the relative magnetic permeability of the material, respectively, while μ_0 is the magnetic permeability of the free space.

C. Source Terms

The coils in the LIM topology are represented as spatially distributed current sheets on the top boundary of the airgap region. The spatial description for all the three phases of the distributed windings, moving together with velocity v , can be

written as a complex Fourier series

$$J_r(x, t) = \sum_{n=-\infty}^{\infty} J_{ph} e^{-j\omega_n x} e^{j(\omega t - \omega_n v t)} + J_{ph} e^{-j\omega_n x} e^{-j\omega_n \frac{2\tau}{3}} e^{jv(\omega t - \omega_n v t + \frac{2\tau}{3})} + J_{ph} e^{-j\omega_n x} e^{-j\omega_n \frac{4\tau}{3}} e^{j(\omega t - \omega_n v t + \frac{4\tau}{3})} \quad (3)$$

with $\omega = 2\pi f$, $\omega_n = (n\pi/\tau)$ and

$$J_{ph} = \frac{-jh_s J}{2\tau\omega_n} [(1 + e^{-j\omega_n \tau_s}) \times (e^{-j\omega_n x_1} - e^{-j\omega_n x_2} - e^{-j\omega_n x_3} + e^{-j\omega_n x_4})]. \quad (4)$$

As shown in Fig. 4, x_1 and x_2 are the coordinates of the positive current sheet of phase B , while x_3 and x_4 are the coordinates of the negative current sheet of phase B . The current sheets are considered as infinitely thin. Hence, the current density J is multiplied by the slot height h_s . As the phases are spatially distributed in sequences B , C , and A , phases C and A are shifted with $(2\tau/3)$ and $(4\tau/3)$ in the x -direction, respectively. To account for the second layer of the winding, both positive and negative current sheets are additionally shifted with one slot pitch τ_s in the x -direction and the resulting components are added to the expression.

D. Vector Potential Solution

Applying the method separation of variables, a general form of the solution to the vector potential is obtained. In the case of the LIM, the vector potential solution is given in a complex form

$$A_z(x, y, t) = \sum_{n=-\infty}^{\infty} (a_n e^{\sqrt{\lambda_n^2} y} + b_n e^{-\sqrt{\lambda_n^2} y}) e^{j\omega_n x} e^{j\omega t} \quad (5)$$

where a_n and b_n are the unknown coefficients for each harmonic, obtained from the applied boundary conditions, as explained in the following section, and:

$$\lambda_n^2 = \omega_n^2 \quad (6)$$

for non-conducting regions, and

$$\lambda_n^2 = \omega_n^2 + j\omega\mu_0\mu_r\sigma \quad (7)$$

for regions containing conductive materials.

For the LFSM topology, the vector potential solution is obtained as

$$A_z(x, y) = \sum_{n=1}^{\infty} -\frac{1}{\omega_n} (q_n e^{\omega_n y} + r_n e^{-\omega_n y}) \cos(\omega_n x) - \frac{1}{\omega_n} (s_n e^{\omega_n y} + t_n e^{-\omega_n y}) \sin(\omega_n x) \quad (8)$$

where q_n , r_n , s_n , and t_n are the unknown coefficients for each harmonic. This provides the coupling of the Fourier regions with the neighboring MEC regions.

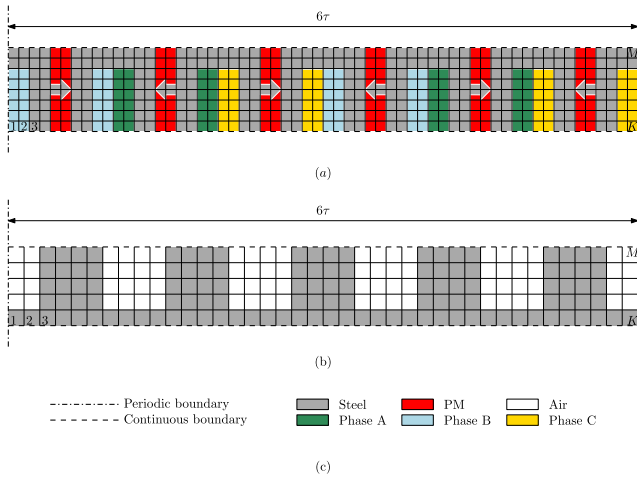


Fig. 6. Discretization of MEC regions. (a) Region II—mover. (b) Region IV—track. (c) Boundaries and materials.

E. MEC

In the LFSM, the regions containing non-homogeneous material properties along the x -direction are modeled using MEC formulation. These regions are discretized in L layers along the y -direction, containing K rectangular elements in each layer. Therefore, a mesh of $M = L \times K$ elements is formed for both the mover and the stator, as shown in Fig. 6(a) and (b), respectively. Each MEC-element encloses one potential node, $\psi(l, k)$, which is defined by four reluctances

$$\mathcal{R}_{xp}(l, k) = \mathcal{R}_{xn}(l, k) = \frac{l_x}{2\mu_0\mu_r^{\text{MEC}}(l, k)S_{zy}} \quad (9)$$

$$\mathcal{R}_{yp}(l, k) = \mathcal{R}_{yn}(l, k) = \frac{l_y}{2\mu_0\mu_r^{\text{MEC}}(l, k)S_{xz}} \quad (10)$$

where l_x and l_y are the lengths of each MEC-element in the x - and y -directions, while S_{zx} and S_{yz} are the cross-sectional areas, parallel to the zx and yz planes, respectively. The values assigned to $\mu_r^{\text{MEC}}(l, k)$ depend on the material in which each element is located. The last element in the x -direction of each layer is coupled with the first element from the same layer in order to fulfill the periodicity in the x -direction.

To obtain correct magnetic behavior inside the MEC-region, the magnetic equivalence of Kirchoff's current law should be fulfilled for each MEC-element. Therefore, all magnetic flux entering one potential node $[\psi(l, k)]$ should be equal to the magnetic flux leaving this node

$$\phi_{xn}(l, k) + \phi_{yn}(l, k) = \phi_{xp}(l, k) + \phi_{yp}(l, k) \quad (11)$$

where

$$\phi_{xp}(l, k) = \frac{\psi(l, kp) - \psi(l, k) + \mathcal{F}_{xp}(l, k) + \mathcal{F}_{xn}(l, kp)}{\mathcal{R}_{xp}(l, k) + \mathcal{R}_{xn}(l, kp)} \quad (12)$$

$$\phi_{xn}(l, k) = \frac{\psi(l, k) - \psi(l, kn) + \mathcal{F}_{xn}(l, k) + \mathcal{F}_{xp}(l, kn)}{\mathcal{R}_{xn}(l, k) + \mathcal{R}_{xp}(l, kn)} \quad (13)$$

$$\phi_{yp}(l, k) = \frac{\psi(lp, k) - \psi(l, k) + \mathcal{F}_{yp}(l, k) + \mathcal{F}_{yn}(lp, k)}{\mathcal{R}_{yp}(l, k) + \mathcal{R}_{yn}(lp, k)} \quad (14)$$

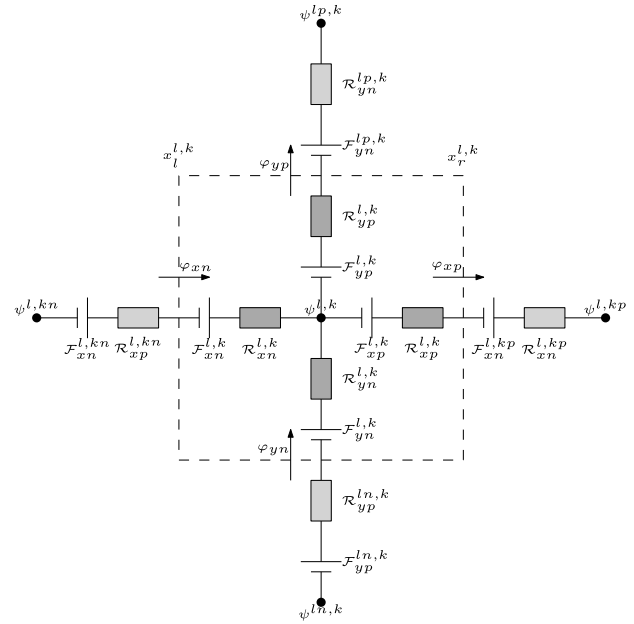


Fig. 7. Single MEC element.

$$\phi_{yn}(l, k) = \frac{\psi(l, k) - \psi(ln, k) + \mathcal{F}_{yn}(l, k) + \mathcal{F}_{yp}(ln, k)}{\mathcal{R}_{yn}(l, k) + \mathcal{R}_{yp}(ln, k)} \quad (15)$$

and the direction of the flux is indicated in Fig. 7.

In the case of Region IV, all source terms are equal to zero, due to the absence of sources in the region. In Region II, the source terms include both PM and coils

$$\mathcal{F}_{\text{PM}}(l, k) = \frac{H_c l_x}{2} \quad (16)$$

$$\mathcal{F}_C(l, k) = \frac{I_{\text{amp}}}{2K_c} \quad (17)$$

where I_{amp} is the current in a single coil, K_c represents the number of MEC elements for a single coil, and H_c is the coercivity of a PM.

F. Magnetic Flux Density Computation

Using the relation

$$\vec{B} = \frac{\partial A_z}{\partial y} \vec{e}_x - \frac{\partial A_z}{\partial x} \vec{e}_y \quad (18)$$

analytical expressions for H_x and B_y are derived from the vector potential solution for each Fourier region. To limit the maximum flux density in the core of the LIM, the magnetic flux density in a single tooth is obtained using

$$B_{\text{tooth}} = \int_{x=x_l}^{x=x_r} \sum_{n=-\infty}^{\infty} -j\omega_n (a_n e^{\lambda_n y} + b_n e^{-\lambda_n y}) e^{j\omega_n x} \quad (19)$$

where x_l and x_r are the coordinates of the tooth in the x -direction.

In the MEC regions, the flux in each part of the MEC-element is obtained after the unknown potentials $\psi(l, k)$ for

each node are calculated. Therefore, the magnetic flux density in the core of the LFSM is calculated according to

$$B_x(l, k) = \frac{\varphi_{xn}(l, k) + \varphi_{xp}(l, k)}{2S_{zy}} \quad (20)$$

$$B_y(l, k) = \frac{\varphi_{yn}(l, k) + \varphi_{yp}(l, k)}{2S_{xz}}. \quad (21)$$

G. Boundary Conditions

To obtain the unknown coefficients in the field description for both topologies, a set of linear equations is solved, accounting the tangential boundary conditions between every two neighboring regions. The LFSM topology is modeled with air above its mover, represented by Region I. In addition, both the LIM and the LFSM are modeled with air regions underneath their tracks, Regions IV and V, respectively. Therefore, the top and bottom boundaries of LFSM and the bottom boundary of LIM are extended to infinity and the Dirichlet boundary condition, forcing all field components to vanish, applies

$$A_z = 0|_{y=\pm\infty}. \quad (22)$$

As the core of the mover is considered as infinitely permeable, a Neumann boundary condition applies to the top of Region I in the LIM topology. However, to account for the source terms, the tangential component of the magnetic field strength at the top boundary of the airgap is equal to the spatially distributed current sheets from (3)

$$H_{xI} = J_\Gamma|_{y=h_s+h_g}. \quad (23)$$

On the border between each two neighboring Fourier regions k and l (e.g., Regions I and II in LIM) located at $y = y_{BC}$, the normal component of the magnetic flux density and the tangential component of the magnetic field strength are continuous

$$B_{yk} = B_{yl}|_{y=y_{BC}} \quad (24)$$

$$H_{xk} = H_{xl}|_{y=y_{BC}}. \quad (25)$$

Similarly, on the boundaries between each Fourier and MEC region, the normal component of the magnetic flux density and the tangential component of the magnetic field strength should also be continuous. To ensure that for the LFSM topology, the continuous boundary conditions become

$$B_y^{\text{HM}} = B_y^{\text{MEC}}|_{y=y_{BC}} \quad (26)$$

$$H_x^{\text{HM}} = H_x^{\text{MEC}}|_{y=y_{BC}}. \quad (27)$$

To adequately define the MEC regions, each element of the bottom layer is coupled with an external flux source underneath the region [$\varphi_{yn}(1, k)$ is separately defined], while the elements from the top layer are coupled with an external flux source at the top of the region [$\varphi_{yp}(L, k)$ is separately defined]. The expressions for the MEC regions are related to a single element, while the resulting equations for the magnetic flux density in Fourier regions are defined for the full periodical section of the analyzed model. To fulfill (26), the harmonic solution for the magnetic flux density in the Fourier region should be represented as multiple flux sources below each

MEC-element from the bottom layer $l = 1$ or above each MEC-element from the top layer $l = L$

$$\varphi_{yn}^{\text{HM}}(1, k) = \iint_S B_y^{\text{HM}}(x, y = y_{BC}) d\vec{S} \vec{x} \vec{z} \quad (28)$$

$$\varphi_{yp}^{\text{HM}}(L, k) = \iint_S B_y^{\text{HM}}(x, y = y_{BC}) d\vec{S} \vec{x} \vec{z} \quad (29)$$

for $1 \leq k \leq K$. By substituting the y -parameter with the corresponding y -coordinate of the boundary between the two coupled regions and considering $x_l(l, k)$ and $x_r(l, k)$ for the left and right edge of a single MEC-element, respectively, the aforementioned equations are rewritten as

$$\varphi_{yn}^{\text{HM}}(1, k) = L_s \int_{x_l(1, k)}^{x_r(1, k)} B_y^{\text{HM}}(x, y = y_{BC}) dx \quad (30)$$

$$\varphi_{yp}^{\text{HM}}(L, k) = L_s \int_{x_l(L, k)}^{x_r(L, k)} B_y^{\text{HM}}(x, y = y_{BC}) dx \quad (31)$$

for $1 \leq k \leq K$, where L_s is the depth of the domain. The normal coupled boundary conditions are defined by (11), taking the form of

$$\varphi_{xn}(1, k) + \varphi_{yn}^{\text{HM}}(1, k) = \varphi_{xp}(1, k) + \varphi_{yp}(1, k) \quad (32)$$

$$\varphi_{xn}(L, k) + \varphi_{yn}(L, k) = \varphi_{xp}(L, k) + \varphi_{yp}^{\text{HM}}(L, k) \quad (33)$$

where the harmonic solutions are substituted in (30) and (31) and integration along the periodical length is performed.

On the same y -coordinate, also the tangential magnetic field strength continuity between the coupled regions should be ensured. The tangential component of the magnetic field along all elements will generate a staircase-shaped function in the x -direction, since (20), calculated for the top or bottom layer of an MEC-region, is considered to be constant within a single element. To derive the coefficients for the adjacent Fourier regions

$$B_x^{\text{MEC}}(y_{BC}) = \sum_{n=-\infty}^{\infty} \frac{1}{6\tau} \int_{x=0}^{6\tau} \sum_{k=1}^K \frac{\varphi_{xn}(l, k) + \varphi_{xp}(l, k)}{2S_{zy}\mu_r^{\text{MEC}}(l, k)} \sin(\omega_n x) dx \quad (34)$$

$$B_x^{\text{MEC}}(y_{BC}) = \sum_{n=-\infty}^{\infty} \frac{1}{6\tau} \int_{x=0}^{6\tau} \sum_{k=1}^K \frac{\varphi_{xn}(l, k) + \varphi_{xp}(l, k)}{2S_{zy}\mu_r^{\text{MEC}}(l, k)} \cos(\omega_n x) dx \quad (35)$$

where 6τ is the full periodical length and $l = L$ or $l = 1$ for the top or bottom layer, respectively. Since the magnetic permeability of MEC region is not homogeneous in the tangential direction, $\mu_r^{\text{MEC}}(l, k)$ is different for each element. By changing the order of summation and integration in the right-hand side of (34), the integration is performed for each MEC-element. Therefore, (27) is fulfilled by substituting the derived equation for B_x from the adjacent Fourier region, which results in

$$\frac{1}{\mu_0} B_x^{\text{HM}}(y = y_{BC}) = \sum_{k=1}^K \frac{1}{\mu_0 \mu_r^{\text{MEC}}(l, k)} B_x^{\text{MEC}}(y = y_{BC}). \quad (36)$$

Finally, two additional linear equations fulfilling (11) for each element inside of the MEC-regions are added to complete the set of boundary conditions and obtain all unknown potentials in MEC-regions. To obtain the unknown Fourier coefficients, the derived equations for H_x and B_y are substituted in the aforementioned boundary conditions and the set of linear equations is solved [13].

H. Force Calculation

The thrust force is derived from Maxwell stress tensor, evaluated inside the airgap, represented by Region II for LIM and Region III for LFSM [14]

$$F_x = \frac{L_s}{\mu_0} \sum_{n=-\infty}^{\infty} \int_0^T B_x(x, y) B_y(x, y) dx \quad (37)$$

where $T = 2\tau$ for LIM and $T = 6\tau$ for LFSM. Taking into account the derived equations for B_x and B_y for Region II, the analytical force equation is rewritten for LIM as

$$F_x = \frac{L_s}{\mu_0} \sum_{n=-\infty}^{\infty} \int_0^{2\tau} [B_{xnII}(y) e^{j\omega_n x} B_{ynII}^*(y) e^{-j\omega_n x}] dx \quad (38)$$

where $*$ is the complex conjugate.

I. Losses Calculation

The copper loss component generated by the armature windings is obtained for both topologies, while the iron losses are neglected. In addition, as the Joule losses in the secondary have a significant effect on the performance of the LIM; they are also included in the loss calculation. Therefore, as the expression for the magnetic vector potential in the conductive region of LIM is available, the losses of its track could be calculated using the Poynting vector approach [15]

$$P_{\text{joule, sec}} = \frac{-L_s}{2} \Re \int_0^{2\tau} E_z H_x^* dx. \quad (39)$$

Only the real component of this expression is taken into account, as it represents the surface power density due to active power flow. The components of this equation are obtained inside the airgap, using the following expressions:

$$E_{zII} = -\frac{\partial A_{zII}}{\partial t} \quad (40)$$

$$H_{xII}^* = \frac{1}{\mu_0} B_{xII}^* = \frac{1}{\mu_0} \frac{\partial A_{zII}^*}{\partial y}. \quad (41)$$

Therefore, after substituting the solution for the vector potential and the derived equation for B_{xII} into (39), the expression for the losses inside the conductive region takes is obtained

$$P_{\text{joule, sec}} = \sum_{n=-\infty}^{\infty} \frac{j L_s \tau \lambda_n^*}{\mu_0} (\omega + \omega_n v) (a_n e^{\lambda_n y} + b_n e^{-\lambda_n y}) \times (a_n^* e^{\lambda_n^* y} + b_n^* e^{-\lambda_n^* y}). \quad (42)$$

For both the LIM and the LFSM, the coils are considered with a single turn. The copper losses generated in the windings are calculated using

$$P_{\text{Cu}} = R_{\text{tot}} I_{\text{rms}}^2 \quad (43)$$

TABLE I
MATERIAL PROPERTIES

Parameter	Symbol	Value	Unit
thermal conductivity of steel	k_{fe}	28	$W/m/K$
thermal conductivity of copper	k_c	1	$W/m/K$
thermal conductivity of PM	k_{PM}	9	$W/m/K$
convection to ambient	h_{conv}	10	$W/m^2/K$
specific copper resistance	ρ	$1.68e^{-8}$	Ωm
conductivity of the Al	σ_{Al}	30	MS/m
conductivity of the iron core	σ_{Fe}	4.5	MS/m
remance of the PMs	B_{rem}	1.2	T
relative permeability of the PMs	$\mu_{r_{pm}}$	1.05	-
relative permeability of the iron core	$\mu_{r_{Fe}}$	5000	-

where

$$R_{\text{tot}} = \rho \frac{L_{\text{tot}}}{A_{\text{coil}}} \quad (44)$$

is the total resistance of all coils in a single periodical section with A_{coil} being the area of a single coil, including the filling factor of the slot, and

$$L_{\text{tot}} = 2L_s + 2L_{\text{end}} \quad (45)$$

where L_s is the depth of the motor and L_{end} is the length of the end-windings. As the LFSM is designed with concentrated coils

$$L_{\text{end}} = w_t + \frac{\pi w_s}{2} \quad (46)$$

while for the LIM, which has distributed windings

$$L_{\text{end}} = \sqrt{(3w_t + 2w_s)^2 + \frac{h_s^2}{4}} + 4w_s + \frac{\pi w_s}{2} \quad (47)$$

where h_s is the height of the slot in the y -direction, and w_t and w_s are the tooth and slot length in the x -direction, respectively.

J. TEC

To avoid demagnetization of PMs in the LFSM topology and permanent damage of the windings in both motors, the temperature level under continuous operation has to be considered. As such, a thermal equivalent circuit (TEC) model is built for the movers of all analyzed topologies, using the same mesh as in MEC [16]. It is assumed that no heat transfer is present at the bottom surface of the primary, where the mover is connected to the airgap. The whole motor is enclosed with a housing. Therefore, thermal convection of the ambient is considered at the top surface of the housing. The ambient temperature is equal to 25°. Thermal conduction is considered inside the movers between all contacting material surfaces [17].

The copper losses, obtained from (43), are injected as heat flux to the center node of each TEC element. The thermal resistances, applied to this model, are as follows:

$$\mathcal{R}_{\text{cond}}(l, k) = \frac{l_x}{k_{\text{cond}} S(l, k)} \quad (48)$$

$$\mathcal{R}_{\text{conv}}(l, k) = \frac{1}{h_{\text{conv}} S(l, k)} \quad (49)$$

TABLE II
GEOMETRICAL PARAMETERS OF LSM TOPOLOGY

Parameter	Symbol	Value	Unit
pole pitch of the PMs	τ_p	12	mm
pole pitch of the phase coils	τ_c	16	mm
back-iron height	h_{sbi}	5	mm
magnet array height	h_{pm}	4	mm
airgap height	h_g	2	mm
slot height	h_s	20	mm
mover height	h_m	25	mm
depth of the domain	L_s	100	mm
total length of mover	L_m	300	mm
fill factor of the coils	k_f	0.6	-

where $S(l, k)$ is the surface on the boundary between two neighboring elements and h_{conv} and k_{cond} are the thermal convection and conduction coefficients, shown in Table I for different material properties.

IV. OPTIMIZATION RESULTS AND DISCUSSION

A. Optimization Assumptions

The optimization objective considered in this paper is to maximize the continuous thrust force. Therefore, the footprint of both LIM and LFSM is fixed to a total mover length of 300 mm and depth of 100 mm, while having the same airgap of 2 mm. The geometric parameters and the main characteristics of the benchmark LSM are listed in Table II. Fixed design parameters for both LIM and LFSM are the overall length, height, and depth of the mover, while their tracks have equal depth and are considered as infinitely long in the x -direction. The optimal pole pitch is not the same for all analyzed topologies, because they have different working principles. Therefore, different values for the pole pitch are considered such that one up to four periodical sections could fit into the overall length of the mover. Each configuration is optimized separately, and the resulting force and losses are multiplied by the number of periodic sections.

The value of the input current density is maximized for each obtained configuration based on the thermal limitations of the performed TEC models to secure the thermal stability of all machines. Therefore, a limit of 100 °C is set as a maximum operating temperature for both motors. As a result of this thermal limit, in the LFSM, the remanence of the PMs is decreased with 0.1% B_{rem} per Kelvin temperature rise. This consideration limits the possible copper losses of the primary, so they cannot exceed the allowed thermal levels. As an addition, for each configuration, the maximum value of the magnetic flux density in the teeth of the mover is limited to be less than 1.5 T. This value is obtained by (19) for the LIM and by (20) and (21) for the LFSM. The performance parameters used for comparison between the LIM and the LFSM are the generated propulsion force, the primary copper losses, and also the Joule losses in the secondary of LIM.

B. Optimization Method and Results

Both the LIM and the LFSM are modeled and optimized using parameter sweep method. In the case of the LIM, the optimization variables are the coil-to-tooth width ratio and the height of the slots in the primary, together with the

TABLE III
OPTIMIZATION RESULTS

Type	Length mm	Periodical sections	J_{peak} A/mm ²	$F_{\text{cont.}}$ N	P_{total} W
LSM	48mm	6	2	183.0	22.3
LIM	300mm	1	1.4	167.4	106.6
	150mm	2	2.1	214.4	128.3
	100mm	3	2.5	184.0	123.8
	75mm	4	2.5	159.9	135.7
LFSM	300mm	1	2.1	287.3	43.2
	150mm	2	1.9	229.2	21.8
	100mm	3	1.7	140.7	24.7
	75mm	4	1.9	121.3	28.9

thickness of the conductive secondary and the optimization is performed, considering the optimal slip frequency for each variation of the pole pitch.

For the LFSM, optimization variables are the ratios between the width of the magnets, coils, and teeth in the mover, together with different configurations for the width and height of the slots. The ratio between the height of the tooth and the height of the yoke in the secondary structure is also included in the optimization process.

The resulting continuous force and losses for the LSM are obtained considering the same thermal constraints and airgap as used for the design of the LIM and the LFSM. Therefore, the results from the optimization are shown in Table III. It could be clearly seen that both the LIM and the LFSM benefit from larger pole pitches, but the losses of the LIM exceed the losses of the LFSM more than twice. This is caused by the additional Joule losses in the conductive secondary of the LIM. The generated thrust force from both topologies is comparable to the benchmark LSM, and at the cost of higher losses, they are suitable as substitutes, considering long-stroke applications.

V. CONCLUSION

This paper has shown the comparison of LIM and LFSM topologies, both of which are optimized for maximum propulsion force while considering their losses. The performance of both the topologies is modeled using fast-converging, semi-analytical modeling techniques. Finally, the results are compared with a benchmark LSM in terms of continuous force and power losses as low-cost alternatives for long-stroke applications.

REFERENCES

- [1] Y. Tang, J. J. H. Paulides, and E. A. Lomonova, "Field weakening performance of flux-switching machines for hybrid/electric vehicles," in *Proc. 10th Int. Conf. Ecologic. Vehicles Renew. Energies (EVER)*, Mar. 2015, pp. 1–10.
- [2] J. Cai, Q. Lu, X. Huang, Y. Ye, and Y. Fang, "Performance investigation of a novel multi-tooth switched-flux linear motor," in *Proc. 10th Int. Conf. Ecologic. Vehicles Renew. Energies (EVER)*, Mar. 2015, pp. 1–7.
- [3] R. Cao and W. Huang, "A double fed three-phase flux-switching linear motor with complementary magnet circuit for urban rail transit," in *Proc. IEEE Conf. Expo Transp. Electrification. Asia-Pacific (ITEC Asia-Pacific)*, Aug. 2014, pp. 1–5.
- [4] S. Wang, D. M. Miao, and J. X. Shen, "Optimal design of a linear induction motor for woodworking machine application," in *Proc. 17th Int. Conf. Elect. Mach. Syst. (ICEMS)*, Oct. 2014, pp. 3633–3637.

- [5] D. Hu, W. Xu, and R. Qu, "Electromagnetic design optimization of single-sided linear induction motor for improved drive performance based on linear metro application," in *Proc. Australas. Univ. Power Eng. Conf. (AUPEC)*, Sep. 2014, pp. 1–6.
- [6] S. Nonaka and T. Higuchi, "Design of single-sided linear induction motors for urban transit," *IEEE Trans. Veh. Technol.*, vol. TVT-37, no. 3, pp. 167–173, Aug. 1988.
- [7] S.-B. Yoon, J. Hur, and D.-S. Hyun, "A method of optimal design of single-sided linear induction motor for transit," *IEEE Trans. Magn.*, vol. 33, no. 5, pp. 4215–4217, Sep. 1997.
- [8] A. Shiri and A. Shoulaie, "Design optimization and analysis of single-sided linear induction motor, considering all phenomena," *IEEE Trans. Energy Convers.*, vol. 27, no. 2, pp. 516–525, Jun. 2012.
- [9] Y. Tang, "Multi-excited reluctance machines: Analysis, modeling, and design for application in electric in-wheel traction," Ph.D. dissertation, Dept. Elect. Eng., Technische Univ. Eindhoven, Eindhoven, The Netherlands, 2017.
- [10] C. H. H. M. Custers, T. T. Overboom, J. W. Jansen, and E. A. Lomonova, "2-D semianalytical modeling of eddy currents in segmented structures," *IEEE Trans. Magn.*, vol. 51, no. 11, pp. 1–4, Nov. 2015.
- [11] J. Gieras, *Linear Induction Drives* (Monographs in Electrical and Electronic Engineering). Oxford, U.K.: Clarendon, 1994.
- [12] K. J. W. Pluk, J. W. Jansen, and E. A. Lomonova, "3-D hybrid analytical modeling: 3-D Fourier modeling combined with mesh-based 3-D magnetic equivalent circuits," *IEEE Trans. Magn.*, vol. 51, no. 12, pp. 1–14, Dec. 2015.
- [13] B. L. J. Gysen, K. J. Meessen, J. J. H. Paulides, and E. A. Lomonova, "General formulation of the electromagnetic field distribution in machines and devices using Fourier analysis," *IEEE Trans. Magn.*, vol. 46, no. 1, pp. 39–52, Jan. 2010.
- [14] M. Amrhein and P. T. Krein, "Force calculation in 3-D magnetic equivalent circuit networks with a Maxwell stress tensor," *IEEE Trans. Energy Convers.*, vol. 24, no. 3, pp. 587–593, Sep. 2009.
- [15] J. H. Poynting, "XV. On the transfer of energy in the electromagnetic field," *Philos. Trans. Roy. Soc. London*, vol. 175, pp. 343–361, Jan. 1884.
- [16] S. D. Sudhoff, *Introduction to Thermal Equivalent Circuits*. Hoboken, NJ, USA: Wiley, 2014, pp. 349–402.
- [17] H. Wong, *Handbook of Essential Formulae and Data on Heat Transfer for Engineers*. London, U.K.: Addison-Wesley, Dec. 1977.